

Interlayer electrodynamics and unconventional vortex state in $\text{YBa}_2\text{Cu}_3\text{O}_y$ A. D. LaForge,^{1,*} W. J. Padilla,^{1,†} K. S. Burch,^{1,‡} Z. Q. Li,¹ S. V. Dordevic,² Kouji Segawa,³ Yoichi Ando,³ and D. N. Basov¹¹*Department of Physics, University of California, San Diego, La Jolla, California 92093, USA*²*Department of Physics, The University of Akron, Akron, Ohio 44325, USA*³*Central Research Institute of the Electric Power Industry, Komae, Tokyo 201-8511, Japan*

(Received 23 March 2007; revised manuscript received 24 May 2007; published 31 August 2007)

We report on the c -axis magneto-optical response of $\text{YBa}_2\text{Cu}_3\text{O}_y$ ($y=6.65$ and 6.75) single crystals, with magnetic fields oriented both parallel and perpendicular to the CuO_2 planes. The dominant characteristic of the c -axis electrodynamics in the superconducting state, the Josephson plasma resonance (JPR), is remarkably sensitive to fairly modest magnetic fields below 8 T. Fields oriented perpendicular to the CuO_2 planes are shown to shift the edge of the JPR and also reduce the weight of the so-called “400-cm⁻¹ mode,” shedding light on this enigmatic feature. In the $H\parallel\text{CuO}_2$ geometry, where the magnetic field initiates Josephson vortices, we observed a strong mode in the far-infrared which hardens with increasing field. The field dependence of the low-frequency resonance behavior is contrasted to that of two other cuprate materials: $\text{La}_{2-x}\text{SrCuO}_4$ compounds that we have investigated earlier, and $\text{Bi}_2\text{Sr}_2\text{CaCu}_2\text{O}_{8-\delta}$. Specifically, there exist disparities in the number and field dependence of longitudinal modes measured for each system. Many of these differences can be explained through a new numerical solution of the interlayer phase equations which includes effects of both in-plane and c -axis dissipation parameters. Support for this approach is given by calculations of the Josephson vortex lattice ground state configuration, and further insight is gained through the phenomenological framework of the transverse JPR model, as well as a classical model of vortex dynamics.

DOI: [10.1103/PhysRevB.76.054524](https://doi.org/10.1103/PhysRevB.76.054524)

PACS number(s): 74.25.Gz, 74.72.-h, 74.50.+r, 74.25.Qt

I. INTRODUCTION

Since the first synthesis of single crystal cuprate superconductors nearly two decades ago, there has been much interest in their interplane conductivity.^{1,2} The coupling between the major structural subunits, the CuO_2 planes, has been shown to be of Josephson origin,³⁻⁵ and interplay has been observed between the phonon modes and the electronic background, both of which reveal complicated temperature dependence.⁶⁻⁸ The formation of the pseudogap in the c -axis electronic conductivity of underdoped crystals⁹⁻¹³ (or of the superconducting gap in nearly optimally doped compounds²) and the local field effects involving the phonon modes¹⁴ yield a rich variety of complex behaviors. Furthermore, observation of phenomena such as the change of kinetic energy below T_c (Refs. 15–20) may give insight into the mechanism of high- T_c superconductivity itself.

Both doping and temperature dependence of the interplane conductivity have been investigated in detail for several families of high- T_c cuprates.^{9,12,19,21} There is an agreement on the gross trends,² although the interpretation of several features, including the so-called “400-cm⁻¹ resonance” seen only in bilayered materials, remains controversial.^{12,22,23}

There has been comparatively little work on the effect of magnetic field on the interlayer transport,²⁴⁻²⁶ with only two publications pertaining to the $\text{YBa}_2\text{Cu}_3\text{O}_y$ (YBCO) system,^{27,28} which is otherwise one of the most studied high- T_c superconductors. This scarcity is an indicator of the technical difficulty of these experiments rather than their importance. Magnetic field constitutes an efficient tuning “knob;” the field can be used to impact the superfluid density more gently than temperature and, unlike doping, this tuning is

reversible and does not change the level of disorder in the system. In this article we exploit the influence of magnetic field to better understand the origin of several characteristics of the vortex state as well as of the anomalies of the c -axis response.

For field magnitudes between the lower and upper critical fields, field lines enter a type-II superconductor in tubes of quantized flux known as vortices. The vortex state, particularly that of the high- T_c cuprates, presents a complex phase diagram characterized by varying degrees of structural order, pinning, and flux flow, among other properties.^{29,30} The current theoretical descriptions of the vortex state have been successful at explaining, and at times even predicting, the phenomena observed in transport and thermodynamic experiments.³¹⁻³³ The results of infrared and microwave measurements as a whole, however, have not been so easily accounted for; as we will show in this article, the data collected for the canonical cuprate families^{25,27,34} reveal distinct electromagnetic responses which have thus far not yielded to description under a single theoretical picture. Here conductivity data for the underdoped YBCO system will be presented and compared with previous experimental results in light of several theoretical perspectives. Section II will describe the magneto-optical experiment carried out at University of California, San Diego. We will present temperature and field dependence of both the reflectance data and the optical constants obtained from them. In Sec. III we will introduce a progression of theoretical models relevant to the interplane electrodynamics, including the vortex dynamical model of Tachiki, Koyama, and Takahashi (TKT),³⁵ the bilayer model by van der Marel and Tsvetkov (vdMT),³⁶ vortex lattice ground state calculations by Nonomura and Hu,³⁷ and a numerical solution of the interlayer phase equations by Koshelev.^{38,39} We singled out Refs. 35, 36, and 38 out of

many other models constructed to describe the vortex dynamics^{40–43} because the TKT, vdMT, and Koshelev scenarios explicitly consider the frequency dependence of the optical constants in the vortex state. The vortex lattice calculations by Nonomura and Hu³⁷ and Koshelev³⁹ define the regimes in which these models are applicable. Each perspective contributes to the understanding of this problem, but we will show that dissimilar features of the Josephson vortex electrodynamics can best be reconciled by considering the role of both in-plane and c -axis dissipation following the recent theoretical treatment by Koshelev.³⁸

II. MAGNETO-OPTICAL EXPERIMENT

A. Raw reflectance data

The single crystals of YBCO under study in this work were grown using the flux method and annealed to oxygen contents of $y=6.65$ and 6.75 . Transport measurements, reported elsewhere,⁴⁴ show that these crystals are of high purity, and sharp transitions to the superconducting state occur at $T_c=60$ K and 65 K, respectively. One large crystal (ac -face area= 2×5 mm²) was used for each zero-field characterization, while for magneto-optical measurements 3–4 smaller samples were assembled to form 3×6 mm² mosaics. Samples were approximately 3 mm thick. For each doping, all samples studied were grown and annealed in the same batch.

Experimental data were collected in a two-step process. Zero-field absolute reflectance $R(\omega)$ was first obtained at near-normal incidence over a broad range of frequency (18–48 000 cm⁻¹) and temperature (8–295 K). In order to minimize the effects of finite sample size the reference data were taken using a technique where a sample is coated in-situ with Au.⁴⁵ Field induced changes of reflectance were then recorded as the ratio $R(T,H)/R(T,0\text{ T})$ for magnetic fields H up to 8 T applied both parallel and perpendicular to the CuO₂ plane. Although the system has been characterized to be stable over changing fields, reference spectra were also collected in field using an aluminum mirror.⁴⁶ In all measurements the electric field was linearly polarized along the c axis of the crystal.

Zero-field reflectance $R(\omega)$ at several temperatures is displayed in Fig. 1(a) for $y=6.67$ and Fig. 2(a) for $y=6.75$. At $T=295$ K the reflectivity is flat in the far infrared with an upturn toward $R=1$ as $\omega \rightarrow 0$. The rich structure above $\omega = 100$ cm⁻¹ due to a series of transverse optical phonons is followed by nearly featureless mid-infrared response. As the temperature is lowered from room temperature to T_c the far-infrared reflectance shifts to lower values, indicating that the system is becoming less conducting in the c direction. A broad feature near $\omega=450$ cm⁻¹ appears at temperatures as high as 150 K and grows dramatically with further cooling. Below T_c a distinct change is seen in the low-frequency spectra; here we observe a sharp plasma edge at $\omega=\omega_B$, below which reflectance is nearly unity. This feature is a signature of the Josephson plasma resonance (JPR), a coherent interplane oscillation of Cooper pairs. This plasma edge grows sharper and moves to higher energy as the supercon-

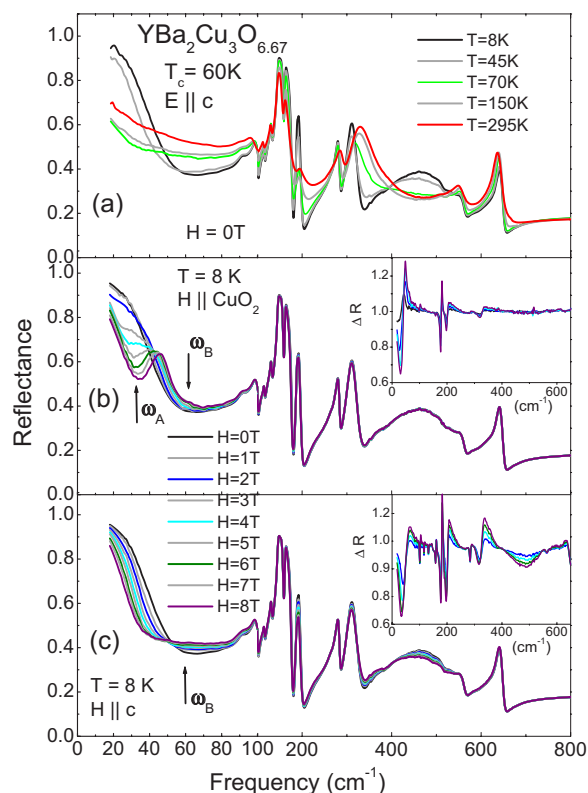


FIG. 1. (Color online) Infrared reflectance $R(\omega)$ of YBa₂Cu₃O_{6.67} single crystal for (a) several temperatures above and below T_c and at 8 K for magnetic fields oriented (b) parallel to the CuO₂ planes and (c) parallel to the c axis. Below T_c the sharp reflectance edge characteristic of the Josephson plasma resonance (JPR) is evident. Fields applied parallel to the CuO₂ planes produce a resonance feature below the plasma edge which shifts upward with increasing field, while c -axis fields shift the JPR to lower energies. The “400 cm⁻¹ mode,” which appears above T_c , is clearly modified by c axis, but not in-plane, magnetic fields. Inset: Field ratios $\Delta R=R(8\text{ K}, H\text{ T})/R(8\text{ K}, 0\text{ T})$.

ducting condensate is stiffened at lower temperatures. These results are consistent with earlier studies of similar dopings.^{9,12}

Application of an external magnetic field in either orientation with respect to the CuO₂ plane produces dramatic changes in reflectance. For measurements made with $H\parallel\text{CuO}_2$, shown in Figs. 1(b) and 2(b), a new absorption feature is observed at frequencies ω_A below the JPR edge. This dip in $R(\omega)$ (first appearing at $\omega_A=40$ cm⁻¹ for $y=6.75$ at $H=4$ T) deepens and moves to higher energies with increasing field. This agrees with optical studies of YB₂Cu₃O_{6.60} in magnetic field.²⁷ Several contrasts between dopings are observed, however. The present $H\parallel\text{CuO}_2$ spectra for the $y=6.75$ crystal do not exhibit the decrease of the JPR edge frequency ω_B seen for the $y=6.60$ and 6.67 dopings. Also, the data reported in this work show no enhancement of the “400 cm⁻¹ resonance,” as was seen in the prior data for $y=6.60$.²⁷ In fact, no new absorptions appear at frequencies higher than 100 cm⁻¹, and the only modifications to the spectra involve minute shifts of phonon peak frequencies. In the $H\parallel c$ geometry, an entirely different behavior is seen [see

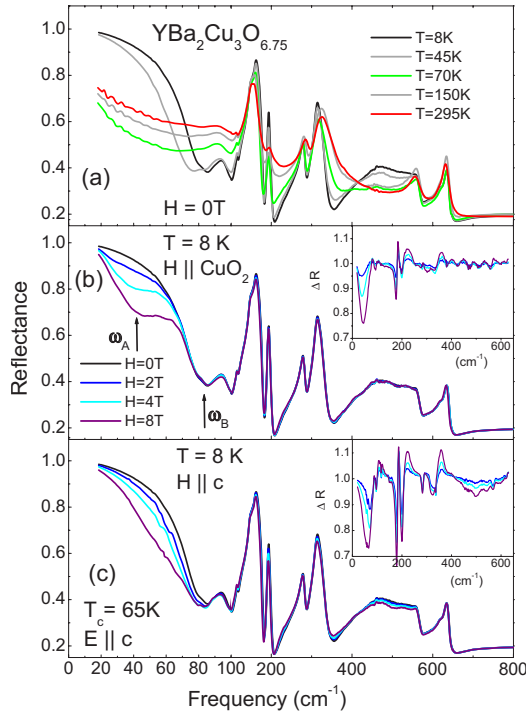


FIG. 2. (Color online) Infrared reflectance $R(\omega)$ of $\text{YBa}_2\text{Cu}_3\text{O}_{6.75}$ single crystal. See caption of Fig. 1 for details.

Figs. 1(c) and 2(c)]. There is no evidence of a new resonance in the low-frequency absorption; instead the JPR edge softens and broadens. The higher energy behavior is also clearly dissimilar between the two experiments, as only the $H\parallel c$ reflectance exhibits a suppression of the “400 cm^{-1} feature.” The differences between the various spectra are highlighted by the field ratios $R(H)/R(H=0)$ in the insets to Figs. 1(b), 1(c), 2(b), and 2(c). For both $H\parallel\text{CuO}_2$ and $H\parallel c$ geometries field induced changes of reflectance became weaker and broader as the temperature was increased to T_c , and in the pseudogap state above T_c no field induced changes were observed within the signal-to-noise of our experiment.

B. c -axis optical conductivity, loss function, and superfluid density

Reflectance data were transformed via the Kramers-Kronig (KK) relations to produce the complex conductivity $\hat{\sigma}(\omega) = \sigma_1(\omega) + i\sigma_2(\omega)$ and complex dielectric function $\hat{\epsilon}(\omega) = \epsilon_1(\omega) + i\epsilon_2(\omega)$. We have verified that the extrapolations required for the KK analysis do not affect the conductivity spectra within the range where actual data exist. Generally, the conventional form of the KK integrals is not suitable for reflectance data collected in magnetic field due to the emergence of nondiagonal components in the conductivity tensor.⁴⁷ In a metal these contributions are governed by the cyclotron frequency $\omega_c = eH/m^*c$, where H is the applied magnetic field and m^* is the electronic effective mass. Since the effective masses relevant to both the intraplane and particularly interplane response of cuprates are large,⁴⁸ the use of the conventional KK relations would be justified. In a

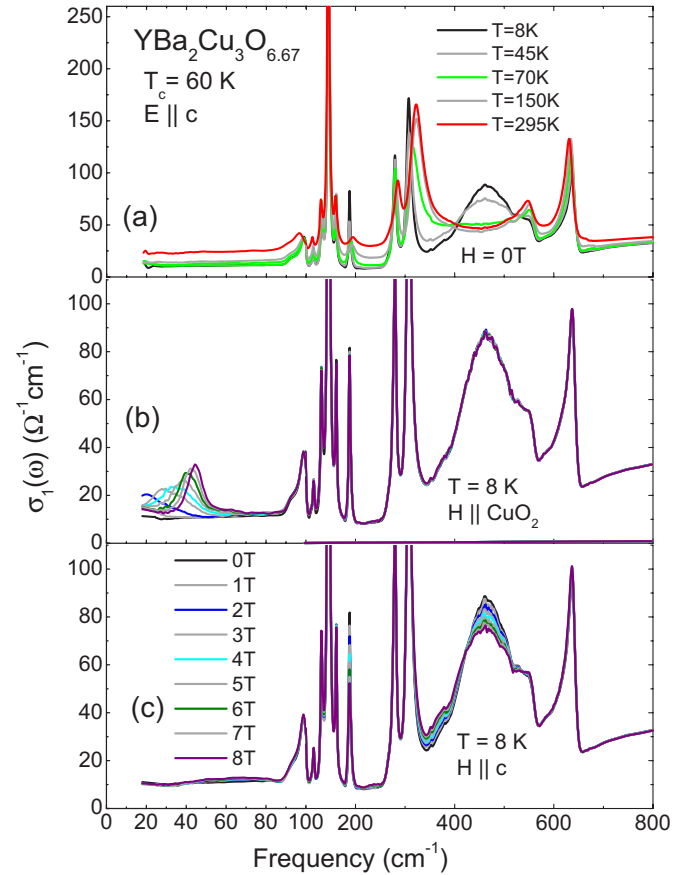


FIG. 3. (Color online) Optical conductivity of $\text{YBa}_2\text{Cu}_3\text{O}_{6.67}$ for (a) several temperatures and at 8 K for magnetic fields oriented (b) parallel to the CuO_2 planes and (c) parallel to the c axis. Similar to $R(\omega)$, the new low-frequency resonance is only seen for in-plane fields. Fields applied along the c axis reverse the effect of lowering temperature by weakening the 400- cm^{-1} mode and restoring spectral weight to the 320 cm^{-1} phonon.

superconductor, however, the relevant parameter is the hall angle, which has been shown to be small both in the plane and along the c axis of YBCO.⁴⁹

The dissipative part of the conductivity, $\sigma_1(\omega)$, is shown in Figs. 3 and 4. At room temperature $\sigma_1(\omega)$ is characterized by a series of infrared active phonons superimposed upon a nearly flat electronic background. The zero-field conductivities, displayed in Figs. 3(a) and 4(a), show that both the phonon structure and electronic background are temperature dependent, with two major effects taking place. First is the emergence of the pseudogap, a partial suppression of low-frequency conductivity common in underdoped cuprates. Also important is the shift in spectral weight from the high-frequency tail of the 320 cm^{-1} phonon to the asymmetrical mode at 450–500 cm^{-1} .⁸ Note that this shift begins at temperatures as high as 150 K, far above T_c . This mode, which appears in a variety of bilayered cuprates, has been attributed to a Josephson transverse mode,³⁶ and alternatively to bilayer splitting.²³ Note that the overall conductivity levels are higher for $y=6.75$ than for $y=6.67$, and that the asymmetrical mode occurs at a higher frequency.

Similar to the raw reflectance data, the optical conductivity displays dramatically different behavior between the two

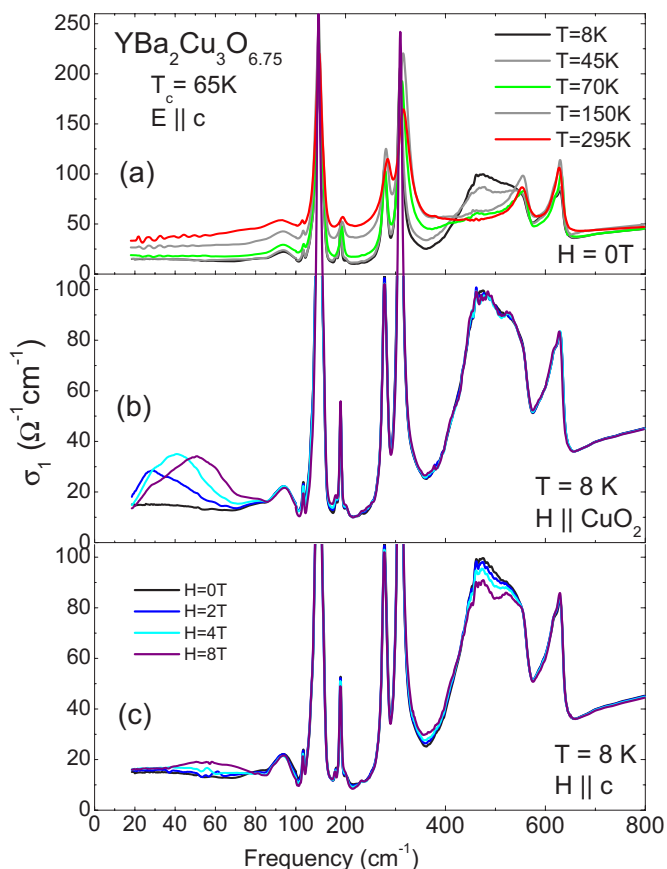


FIG. 4. (Color online) Optical conductivity $\sigma_1(\omega)$ of $\text{YBa}_2\text{Cu}_3\text{O}_{6.75}$ single crystal. See caption of Fig. 3 for details.

field orientations studied. For $H\parallel\text{CuO}_2$, shown in Figs. 3(b) and 4(b), the low frequency dip seen in the reflectance spectra is manifested in $\sigma_1(\omega)$ as a resonance whose strength and center frequency depend on magnetic field. In contrast, the $H\parallel c$ conductivity changes very little in the low-frequency region [see Figs. 3(c) and 4(c)]. The contribution due to the electronic background increases monotonically with field, and only a broad absorption is seen. Significant field-induced changes do appear at higher energies, however, as the “400 cm^{-1} ” mode is systematically suppressed with $H\parallel c$. Spectral weight is transferred back into the edge of the 320 cm^{-1} phonon, reversing the effects of lowering temperature.

Further insight into the field dependence of the JPR can be gained by examining the loss function $\text{Im}[-1/\epsilon(\omega)]$, shown in Figs. 5 and 6. Peaks in the loss function occur at possible zero crossings of $\epsilon_1(\omega)$, identifying the screened frequency position of longitudinal plasma oscillations. The low-frequency loss function spectra in Figs. 5(a) and 6(a) are mainly featureless at temperatures above the superconducting transition, but below T_c they exhibit a resonance at $\omega_B = 50(77) \text{ cm}^{-1}$ which corresponds to the longitudinal JPR in the $y=6.67$ (6.75) sample. As the field applied parallel to the planes is increased a new peak develops at a lower frequency $\omega_A = 30(40) \text{ cm}^{-1}$ [see Figs. 5(b) and 6(b)]. In the more underdoped sample the main loss function peak hardens by 5 cm^{-1} by 4 T, but does not change as field is increased to

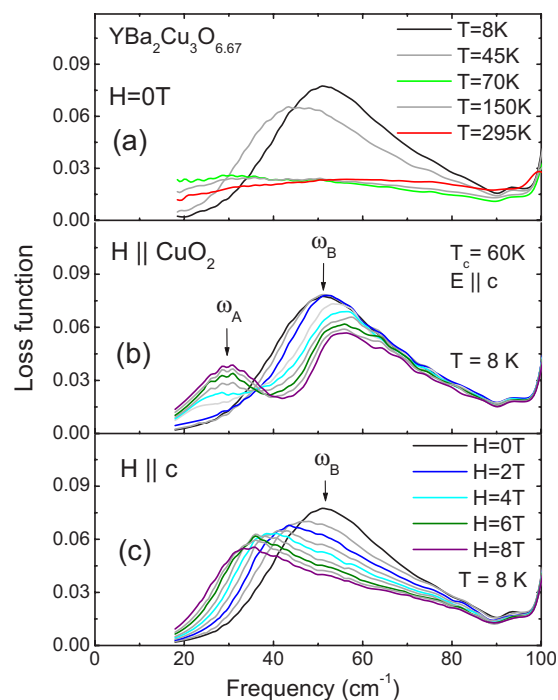


FIG. 5. (Color online) Loss function for $\text{YBa}_2\text{Cu}_3\text{O}_{6.67}$ for (a) several temperatures above and below T_c and at 8 K for magnetic fields oriented (b) parallel to the CuO_2 planes and (c) parallel to the c axis. Peaks in the loss function generally identify electromagnetically active ionic motions along the c axis, such as longitudinal plasma oscillations and phonons. In the normal state, phonon peaks can be identified above 90 cm^{-1} . Below T_c a strong new peak at $\omega_B = 50 \text{ cm}^{-1}$ indicates the presence of the Josephson plasma resonance (JPR). A second peak emerges near $\omega_A = 30 \text{ cm}^{-1}$ in fields parallel to the CuO_2 planes, and the JPR peak broadens and weakens for fields parallel to the c axis.

8 T. At the higher doping the main peak frequency is field independent. This additional mode does not appear for $H\parallel c$ in Figs. 5(c) and 6(c); rather, the original peak at ω_B is shifted to lower energies, reflecting the suppression of the JPR.

We will now show that the dominant effect underlying the trends in the optical conductivity seen above is a destruction of the superconducting condensate by magnetic field. The electronic response of a superconducting material can be quantified within a two-fluid framework in which the optical conductivity has the form $\sigma_1(\omega) = \rho_s \delta(\omega) + \sigma_1^{\text{reg}}(\omega)$. The first term stands for the contribution of the superconducting condensate, which has the form of a zero-frequency delta function whose weight is the superfluid density $\rho_s = \pi e^2 n_s / 2m^*$. Here n_s is the superconducting carrier density and m^* is the pair effective mass. The latter term is the regular, finite-frequency contribution $\sigma_1^{\text{reg}}(\omega)$ due to unpaired carriers and pinned vortex modes, among other sources. The δ function cannot be directly observed in the $\sigma_1(\omega)$ spectra, but its influence can be deduced by examining $\sigma_2(\omega)$. This virtue of imaginary conductivity is due to Kramers-Kronig relations implying that the δ function in $\sigma_1(\omega)$ must be matched with a $1/\omega$ dependence in $\sigma_2(\omega)$. The net outcome of the condensate formation is the following expression for the imaginary conductivity:

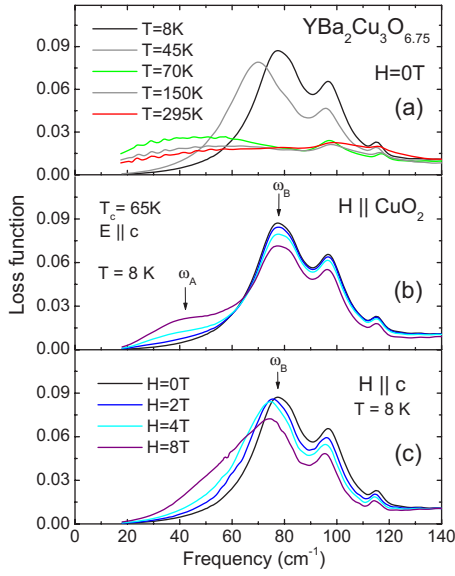


FIG. 6. (Color online) Loss function for $\text{YBa}_2\text{Cu}_3\text{O}_{6.75}$ single crystal. See caption of Fig. 5 for details.

$$\sigma_2(\omega) = \frac{\rho_s}{\pi\omega} + \sigma_2^{\text{reg}}(\omega). \quad (1)$$

Similar to the real conductivity, the spectra of $\sigma_2(\omega)$ inferred from KK analysis of the data also contain a contribution due to unpaired carriers and pinned vortex modes in addition to the superfluid term. Therefore, in order to extract accurate values of the superfluid density from the conductivity data it is imperative to correct the results of the KK analysis for this regular contribution $\sigma_2^{\text{reg}}(\omega)$.⁵ Equation (1) can then be solved for the corrected superfluid density $\rho_s = \pi\omega[\sigma_2(\omega) - \sigma_2^{\text{reg}}(\omega)]$, which is plotted for $\text{YBa}_2\text{Cu}_3\text{O}_{6.75}$ in Fig. 7 for $H=0-8$ T and several temperatures below T_c . As emphasized by the 3D nature of the graph, the increases of temperature and field share the common aspect of suppressing ρ_s , but with disparate power law dependencies. Different power laws are also observed between the two field geometries; although ρ_s is suppressed by 50% at 8T in both cases, the field dependence of ρ_s in the $H\parallel\text{CuO}_2$ orientation [Fig. 7(a)] has a concave curvature whereas the $H\parallel c$ suppression [Fig. 7(b)] is nearly linear in field. The crystal with $y=6.67$ (not shown) exhibited similar trends of suppression of superfluid, but with smaller magnitudes.

C. Comparison to other cuprate superconductors

To place into context the electrodynamic response of the $\text{YBa}_2\text{Cu}_3\text{O}_y$ compounds described above, it is useful to make a comparison to two other cuprate superconductors, $\text{La}_{2-x}\text{Sr}_x\text{CuO}_4$ (La214) and $\text{Bi}_2\text{Sr}_2\text{CaCu}_2\text{O}_{8+d}$ (Bi2212). We will show that despite the common structural characteristics of these compounds, their Josephson vortex state electrodynamic exhibit striking differences. Consider, for example, the c -axis optical properties of La214 crystals under magnetic field applied parallel to the CuO_2 planes. The reflectance, shown in Fig. 8(b), shows no sign of the structure at $\omega = \omega_A$ seen in YBCO. Rather, the JPR frequency ω_B softens

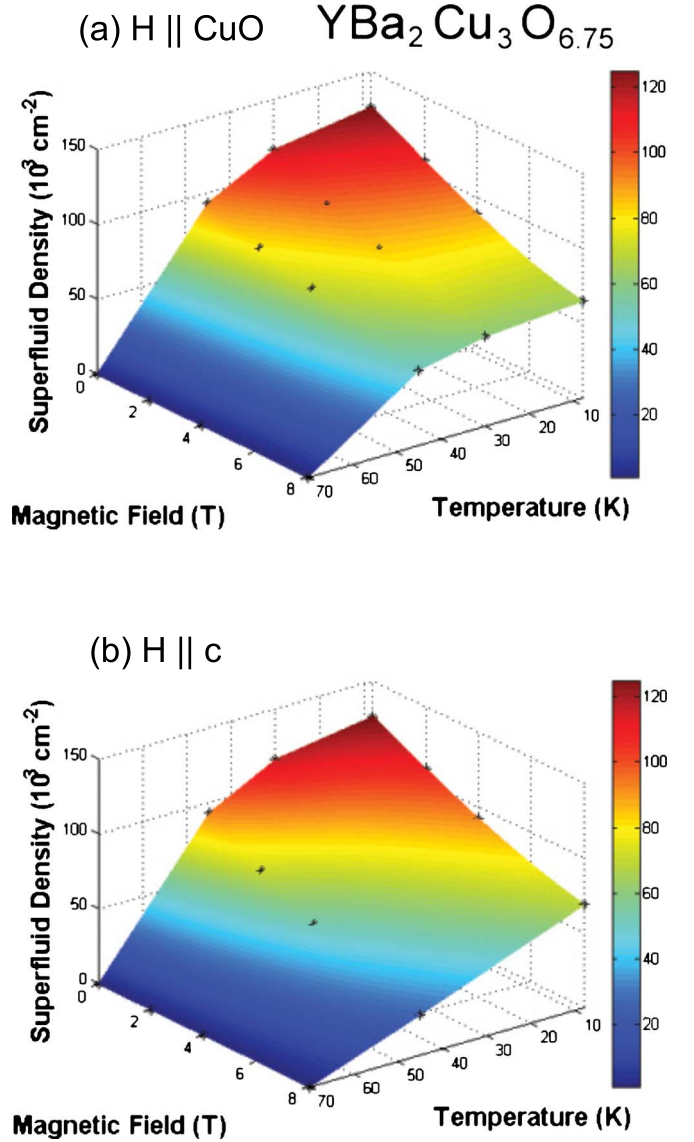


FIG. 7. (Color online) Superfluid density ρ_s for $\text{YBa}_2\text{Cu}_3\text{O}_{6.75}$, determined by σ_2 analysis with correction for regular contribution, as a function of temperature and magnetic field. Although both plots show suppression of superfluid density with field, the parallel field orientation (a) produces a concave curvature, while the perpendicular field dependence (b) is nearly linear.

and the entire plasmon structure is weakened. Stark differences also appear in the low frequency optical conductivity, plotted above in Figs. 3(b) and 4(c) for YBCO and published elsewhere for La214.⁵⁰ In contrast to the behavior observed for YBCO, $\sigma_1(\omega)$ increases broadly with field for La214, with no formation of a sharp transverse resonance.

In the Bi2212 system the larger anisotropy lowers the JPR frequency to a range inaccessible to infrared spectroscopy; microwave magnetoabsorption techniques are used instead.⁵¹ Since the latter method identifies longitudinal modes, the features it reveals can be most directly compared to the loss function in the above IR results. The work in Ref. 51 focused on an underdoped crystal with transition temperature $T_c = 70$ K, but all trends were observed at optimal doping as well. The frequency-field diagram for Bi2212 in Fig. 8(e)

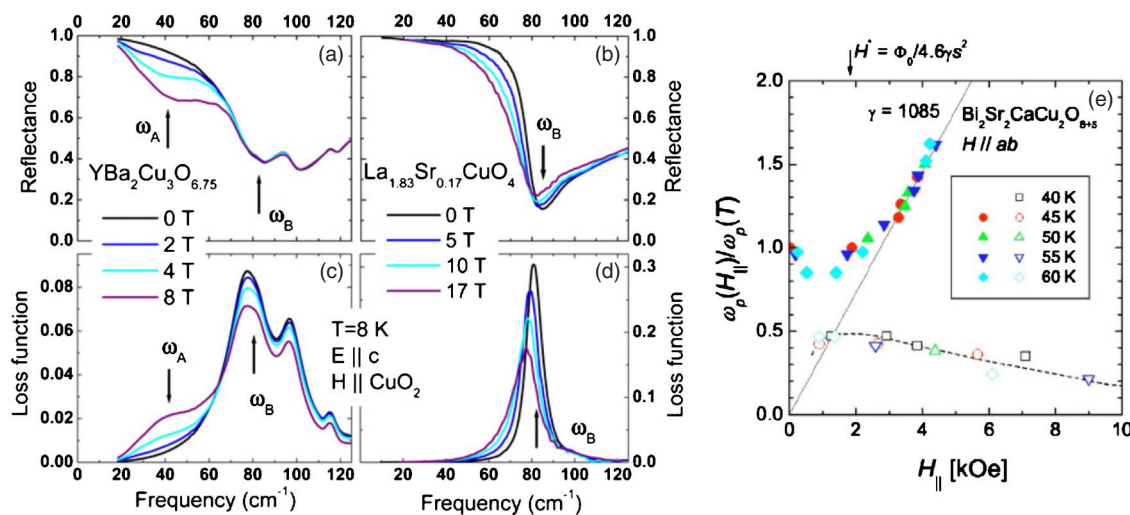


FIG. 8. (Color online) Comparison of electrodynamic response data for various families of cuprate superconductors. Raw reflectance spectra reveal a resonance feature below the Josephson plasma edge for YBCO (a) but not La214 (b). The loss function spectra show two longitudinal resonance modes for YBCO (c), but only one for La214 (d). A frequency-field phase diagram for Bi2212 (e) from Ref. 51 displays two magnetoabsorption modes.

displays two resonances: one appears only at higher temperatures and hardens linearly with parallel field as a dense vortex lattice is formed;⁴² the other resonance, visible at low temperature and nonzero fields, softens with magnetic field. This result differs distinctly from that of the other systems; La214 supports only one sharp longitudinal mode, and its peak frequency ω_B decreases with field [see Fig. 8(d)]. As mentioned above, in YBCO the JPR peak frequency ω_B is field independent or weakly increasing, and the linewidth is broader [see Fig. 8(c)]. Furthermore, both modes in YBCO are sharpest at low temperature, with no evidence of the additional temperature scale seen in Bi2212. The closest agreement between the data sets is in the lower-frequency modes of YBCO (labeled as ω_A) and Bi2212. Both are too weak to be resolved at the lowest fields and have little frequency dependence in modest fields. At the outset, the electromagnetic responses of the three systems appear to be quite distinct and without a common pattern; thus, the task of finding a universal explanation has not been straightforward.^{52–55}

III. THEORETICAL MODELS

Many theoretical models have been proposed to explain the low-frequency infrared and microwave properties of the layered high- T_c superconductors. Earlier theories^{40,41,43} have accurately described elements of the experimental data for individual families of cuprates but have not sufficiently accounted for the differences in resonance behaviors from family to family displayed in Fig. 8. Discussion below outlines a series of developments which form a coherent explanation of these disparities. All models discussed give predictions for the frequency dependence of the optical conductivity. In subsection A, a classical description of Josephson vortex oscillation presented by Tachiki, Koyama, and Takahashi (TKT)³⁵ marks a good starting point for approaching this problem. Here the interlayer phase equations are solved analytically for small fields. A different perspective is gained in Sec. III B

with the phenomenological model of van der Marel and Tsvetkov,^{36,56} which considers the modification of the JPR behavior in a multilayer system. The parameter space where this model is applicable is specified in detail by calculations of the Josephson vortex lattice ground state, computed by Nonomura and Hu,³⁷ as well as Koshelev,³⁹ and discussed in Sec. III C. This knowledge of the ground state configuration has been integrated into new numerical solutions of the interlayer phase equations which take into account the in-plane and c -axis dissipations. This approach by Koshelev³⁸ is described in Sec. III D.

A. Vortex oscillation model

Any microscopic derivation of the electrodynamic properties of a coupled Josephson system must begin with the interlayer phase equations,^{57,58} and it is instructive to first consider their analytical solution. With this objective, we have found many of the features of the low-frequency resonance mode to be in qualitative, and perhaps even quantitative, agreement with predictions of the vortex dynamics model of TKT.³⁵ This theory has been applied to explain changes in superfluid density and plasma edge position in LSCO,^{24,25} but the present work is the first to employ it to fit a finite-frequency mode in the conductivity data. The TKT model offers descriptions of the low frequency electromagnetic response of cuprate superconductors for magnetic fields oriented both parallel and perpendicular to the CuO_2 planes, taking into account the difference in vortex structure between the two geometries. For the case of magnetic fields oriented parallel to the c axis, the flux penetrates the material by forming pancake vortices which order in an Abrikosov lattice in the ab plane.²⁹ According to the TKT model, since the c -axis plasma induced by the applied electric field does not couple to these pancake vortices, the primary effect of the field on the low-frequency optics is quasiparticle scattering inside the normal vortex core and the change in dielectric

function this engenders. The normal and superconducting areas of the ab plane are modeled with oscillators with and without damping, respectively, and the total dielectric function is a weighted average of the two regions. Thus, for low temperatures, we have

$$\varepsilon(\omega) = \varepsilon_c - \frac{\omega_p^2}{\omega(\omega + i0^+)} \left[1 - \frac{H}{H_{c2}} \right] - \frac{\omega_p^2}{\omega(\omega + i\gamma)} \left[\frac{H}{H_{c2}} \right], \quad (2)$$

where H is the applied magnetic field, H_{c2} is the thermodynamic upper critical field, γ is the quasiparticle scattering rate in the normal region, and ω_p is proportional to the total number of carriers.

Fields applied parallel to the ab plane, however, will create Josephson vortices with cores pinned in the normal regions between CuO_2 planes and current patterns sustained by Josephson tunneling. Here the vortex dynamics play an important role, and the equation of motion for a vortex oscillating with viscous damping constant η and mass M about a pinning site with Labusch constant κ_p is

$$M\ddot{u} + \eta\dot{u} + \kappa_p u = \frac{\Phi_0}{c} \vec{J} \times \hat{n},$$

where Φ_0 is the flux quantum, \vec{J} is the current, and \hat{n} is the unit vector along the vortex direction. Solving for the transverse dielectric function yields

$$\varepsilon(\omega) = \varepsilon - \frac{\frac{\omega_{ps}^2}{\omega^2} + \frac{\omega_{pn}^2}{\omega(\omega + i\gamma)}}{1 + \frac{\phi_0}{4\pi\lambda_c^2 \kappa_p - i\eta\omega - M\omega^2}}, \quad (3)$$

where $\omega_{ps} = \sqrt{c^2/\lambda_c^2}$ and ω_{pn} are the superconducting and normal state plasma frequencies, respectively, and λ_c is the c -axis penetration depth. Representative $R(\omega)$ and $\sigma_1(\omega)$ obtained from this model are shown in Fig. 9. Note that the dip in $R(\omega)$ and peak in $\sigma_1(\omega)$ appear only for the $H\parallel\text{CuO}_2$ orientation, as was observed in the experimental data. The $H\parallel c$ spectra exhibit a shift in the frequency of the plasma edge in $R(\omega)$ and a monotonic increase of $\sigma_1(\omega)$, also corresponding to the data. One aspect of the $H\parallel c$ data not accounted for in the TKT theory is the broad absorption near 60 cm^{-1} at $H=8 \text{ T}$. This feature, different in appearance from the resonance seen for $H\parallel\text{CuO}_2$, may be a result of the in-plane inhomogeneities produced by pancake vortices and their random fluctuations in the vortex liquid state.^{50,59}

The TKT functional forms for $R(\omega)$ generated from Eqs. (2) and (3) were successfully fitted to the perpendicular and parallel field experimental data, respectively, for the $y = 6.75$ sample. In the $H\parallel c$ case we used the mean-field $H_{c2} = 41 \text{ T}$ obtained from magnetoresistance measurements⁶⁰ and fit for ω_p and γ . The theoretical agreement is closest for the lower fields, as the 8 T data shows a stronger suppression of the plasmon than theory predicts. For $H\parallel\text{CuO}_2$ the fitting was performed in the following way: first, zero-field $R(\omega)$ was fitted using λ_c and ω_p as free parameters. Next, in-field curves were iteratively fitted with κ_p and η , then λ_c , allowed

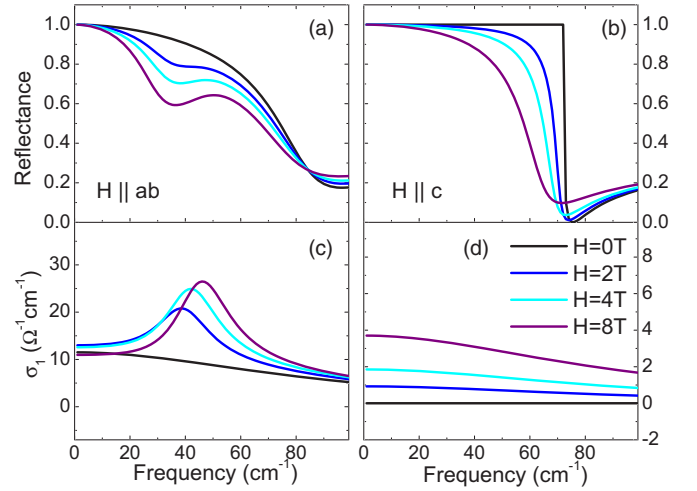


FIG. 9. (Color online) Theoretical model curves for c -axis reflectance and optical conductivity, as derived from the vortex dynamical model of Tachiki, Koyama, and Takahashi [Eqs. (2) and (3)]. Here the penetration depth is adjusted with field to account for the suppression of superfluid density in field. Qualitative trends seen here mirror those seen in the experimental data in Figs. 1 and 2. For $H\parallel\text{CuO}_2$, the low frequency resonance is visible in (a) the reflectance and (c) the optical conductivity. Such a feature is only produced for a large vortex mass. In the $H\parallel c$ orientation, the plasma edge in the reflectance (b) is shifted to lower energies with field. The normal vortex cores increase dissipation in $\sigma_1(\omega)$ (d).

to vary. A single value of M was acceptable for all fields. The regular (nonsuperconducting) components of $\sigma_1(\omega)$ and $\sigma_2(\omega)$ were added to the theoretical prediction to compensate for the presence of phonons and electronic background, which are not accounted for by the model.

When comparing the fit curves to the data in Fig. 10, remarkable agreement is observed in both field and frequency dependency of the resonance. Though not shown, the corresponding peak in $\sigma_1(\omega)$ is also reproduced. As seen in

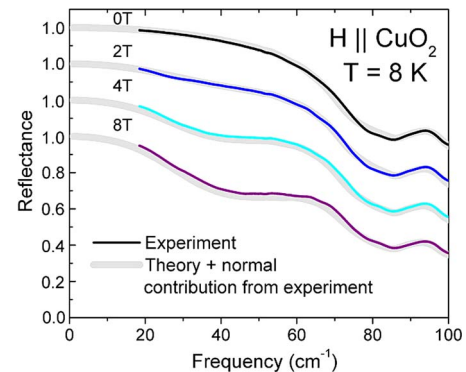


FIG. 10. (Color online) Theoretical fits (thick gray) to experimental reflectance data for $\text{YBa}_2\text{Cu}_3\text{O}_{6.75}$ at 8 K (thin colored) using vortex dynamical model of Tachiki, Koyama, and Takahashi. Several values of magnetic field applied parallel to the CuO_2 planes are shown. For these fits the normal contribution $\sigma_1^{\text{ns}}(\omega)$ was added to the optical conductivity derived from the theory in order to account for phonons and electronic background. Fit parameters are listed in Table I.

TABLE I. Parameters used for fitting reflectance data with TKT theory, as shown in Fig. 8.

H (T)	0	2	4	8
λ_c^{obs} (μm)	4.42	4.80	5.26	6.16
λ_c^{fit} (μm)	4.14	4.14	4.42	4.85
$(\lambda_c^{\text{obs}} - \lambda_c^{\text{fit}}) / \lambda_c^{\text{obs}}$	0.06	0.14	0.16	0.21
ω_p (cm^{-1})	386	358	324	271
κ ($\times 10^6$ Pa)		5.81	5.12	6.15
η ($\times 10^5$ Pa cm^{-1})		1.72	1.18	1.07
M (Pa cm^{-2})		3190	3190	3190

Table I, best-fit values for $\lambda_c(8T)$ were within 20% of those measured experimentally, with better agreement at lower fields, and vortex dynamical parameters κ_p and η were within the range of those reported elsewhere.³⁰ The exception was the vortex inertial mass, which was required to be much larger (factor of 10^4) than theoretically predicted for fields oriented parallel to the planes of a layered superconductor.⁶¹ Since there exists no widely accepted method for determining the vortex mass,^{62–65} it is difficult to interpret the large value of the mass required to reproduce the experimental line shape.

The success of these fits should be tempered with some criticism. The TKT analysis depends sensitively on the dynamical parameters, which can only be corroborated with transport or microwave resonance experiments. It is unclear whether values obtained via these methods should be compatible with those inferred optically, so they were allowed to vary in the fitting. Thus, the fact that the vortex dynamical theory yields such an accurate fit to the data is hardly surprising, given the extra degrees of freedom allowed in the fit. A more fundamental issue is that the application of the TKT model to these systems relies on assumptions which may be invalid. First, the TKT model will produce a new field-induced resonance only if large effective mass is assigned to Josephson vortices. In related work in LSCO,²⁵ vortex-induced suppression of superfluid density was explained through the TKT theory; as shown above no finite frequency feature was observed, and little or no mass was needed to produce a fit. Then within this framework one has to assume massive vortices in YBCO and much lighter ones in La214, an unlikely premise given the similarities in the zero-field response between the two systems, and the parameters upon which vortex mass is theorized to depend. Second, it is likely that the approximations for low frequencies and fields place the features under consideration outside of the physically meaningful parameter space. Nonetheless, the TKT theory affords insight into the influence of the vortex dynamical parameters and provides a good theoretical starting point.

B. Transverse plasmon model

The van der Marel–Tvetskov (vdMT) model was developed specifically to describe the electrostatics of multilayer superconductors.³⁶ It predicts that in a system composed of layers with alternating Josephson coupling

strengths the out-of-phase charge oscillations between layers will produce a transverse optical plasma resonance. A mode of this type is manifested as a resonance in the optical conductivity spectra. This theory was originally introduced as a possible explanation for the anomalously broad “400 cm^{-1} resonance” observed in underdoped bilayered cuprates.^{9,56} The centrality of the compounds’ bilayer nature is supported by the fact that the feature has not been observed in single-layer cuprates such as LSCO. However, when LSCO is doped with Sm a bilayer structure is created, and with it an transverse resonance near 12 cm^{-1} . Calculations based on frequency positions of the longitudinal plasmons within the constituent layers have been used to accurately track the position of the transverse plasmon through changes in temperature^{66,67} and field.⁶⁸

Following this progression, the theory has also been extended to the vortex state of YBCO under a magnetic field applied parallel to the CuO_2 layers.²⁷ The key assumption in this case is that vortices will penetrate only some of the layers, forming a quantized lattice along the c axis with a lattice parameter commensurate with the interlayer spacing.⁴⁰ The differing couplings between junctions with and without vortices then define a vortex superstructure and a transverse resonance is produced. Although the pertinent resonance features in these three systems (YBCO intrinsic bilayer, $\text{Sm}_2\text{O}_2/(\text{La,Sr})_2\text{O}_{2-\delta}$ superlattice, and YBCO vortex superstructure) occur over different energy scales and exhibit strikingly different temperature and magnetic field response, all have been explained using the fundamental idea of the transverse resonance.³⁶

In a derivation of the dielectric function due to a transverse plasmon,³⁶ the bilayer system is modeled as a stack of superconducting layers with alternating Josephson coupling strengths and corresponding plasma frequencies ω_{pA} and ω_{pB} . By adding in series the impedances of the individual layers (rather than the conductivities, as is the case for parallel conduction channels) the dielectric function can be expressed in the form

$$\frac{\varepsilon(\omega)}{\varepsilon_\infty} = \frac{z_A \omega^2}{\omega(\omega + i\gamma_A) - \omega_{pA}^2} + \frac{z_B \omega^2}{\omega(\omega + i\gamma_B) - \omega_{pB}^2}, \quad (4)$$

where ε_∞ is the high-frequency dielectric constant, and ω_{pv} and γ_v are the screened Josephson plasma frequencies and damping constants which characterize each type of junction. The zeros of this function correspond to longitudinal plasma oscillations, which can be observed as peaks in the loss function $\text{Im}[-1/\varepsilon(\omega)]$. A pole in the dielectric function at $\omega_T = (z_A \omega^2 + z_B \omega^2)^{1/2}$ identifies a transverse plasmon and appears as a resonance peak in $\sigma_1(\omega)$. In the simplest form of the bilayer model, the weight factors z_v (constrained by $z_A + z_B = 1$) are determined solely by the volume fractions occupied by the layers, but the theory has been expanded to include the influence of electronic compressibility.⁶⁹

The transverse plasmon formalism has been applied to the present YBCO data for fields parallel to the CuO_2 planes, with all relevant parameters listed in Table II. Examination of the loss function and conductivity spectra in Figs. 3–6 yields, for a fixed magnetic field, the longitudinal plasma

TABLE II. Parameters used for fitting reflectivity with transverse plasmon model [Eq. (4)]. The only free parameters were γ_A and γ_B . All others were inferred from the experimental data in Figs. 2 and 3, as described in the text. The theoretical curves which utilize these parameters are displayed in Fig. 5.

	$y=6.75$		$y=6.67$				
H (T)	8	4	5	6	7	8	
ω_A (cm^{-1})	40	30	30	30	30	30	
ω_B (cm^{-1})	80	55	55	55	55	55	
ω_T (cm^{-1})	52	34	39	40	42	45	
z_A	0.23	0.12	0.29	0.34	0.41	0.53	
z_B	0.77	0.88	0.71	0.66	0.59	0.47	
γ_a (cm^{-1})	25	8.9	13	12	13	15	
γ_b (cm^{-1})	39	32	25	24	23	19	
S_T^{calc} (10^3 cm^{-2})	58	40	40	39	37	35	
S_T^{obs} (10^3 cm^{-2})	59	37	38	38	38	37	

frequencies ω_B and ω_A , corresponding respectively to JPRs in junctions with and without vortices, as well as the transverse plasma frequency ω_T . The proximity of a phonon peak at $\omega=94 \text{ cm}^{-1}$ introduces at most a systematic error of 5% in ω_B for the more highly doped sample. From these frequency positions the weight factors z_A and z_B can be calculated. The high-frequency limit of the experimental $\epsilon_1(\omega)$ is also taken directly from the data. The theoretical reflectivity corresponding to Eq. (4) was fitted to the $R(\omega)$ data, with the damping constants γ_v as the only free parameters. As seen in Fig. 11, the fit matches well the shapes of $R(\omega)$ and $\sigma_1(\omega)$, and the theoretical integrated spectral weight of the transverse mode S_T^{calc} is close to the observed value of S_T^{exp} . For example, for $y=6.75$ we find $S_T^{\text{calc}}=5.88 \times 10^4 \text{ cm}^{-2}$ and $S_T^{\text{exp}}=5.93 \times 10^4 \text{ cm}^{-2}$. Fits were obtained at 4–8(8) T for the crystal with $y=6.67$ (6.75); below these fields the frequency position of the lower longitudinal mode is not well defined, precluding similar quantitative analysis.

Provided the structural parameters of the bilayer crystal are known, then it is possible to calculate the electronic compressibility from the weight factors z_v .^{68,70} In the case of a vortex superstructure, however, we have no separate measurement of the c -axis vortex lattice constant, and the effects of the changing lattice structure and compressibility cannot be deconvoluted.

The observed effects of magnetic field upon the 400 cm^{-1} mode are also in qualitative agreement with the transverse plasmon description. As detailed in the introduction to the vdMT theory, this mode has been described as a transverse plasmon arising from out of phase oscillation of the JPR and another, broader longitudinal mode at a higher frequency. Since the frequency position and spectral weight of the 400 cm^{-1} transverse mode (see Fig. 2) are dependent upon the positions of the longitudinal modes (see Fig. 3), one could expect to see correlations between these entities as they are altered by the field. Indeed, for the $y=6.75$ sample any changes in the position of the loss function peak ω_B corresponding to the Josephson plasmon are linked to changes in the 400 cm^{-1} mode. For $H \parallel \text{CuO}_2$, ω_B and the 400 cm^{-1} mode are both not affected. When H is applied along the c axis, however, we observe a softening of ω_B ,

matched by a suppression of the 400 cm^{-1} mode. For the more underdoped sample, the hardening of the loss function mode at $\omega=\omega_B$ is not matched by a growth of the 400 cm^{-1} mode. This may suggest that both low frequency longitudinal modes are involved in the out-of-phase coupling which produces the broad transverse mode, and that the hardening of the mode at ω_B is balanced by the growth of the one at ω_A to

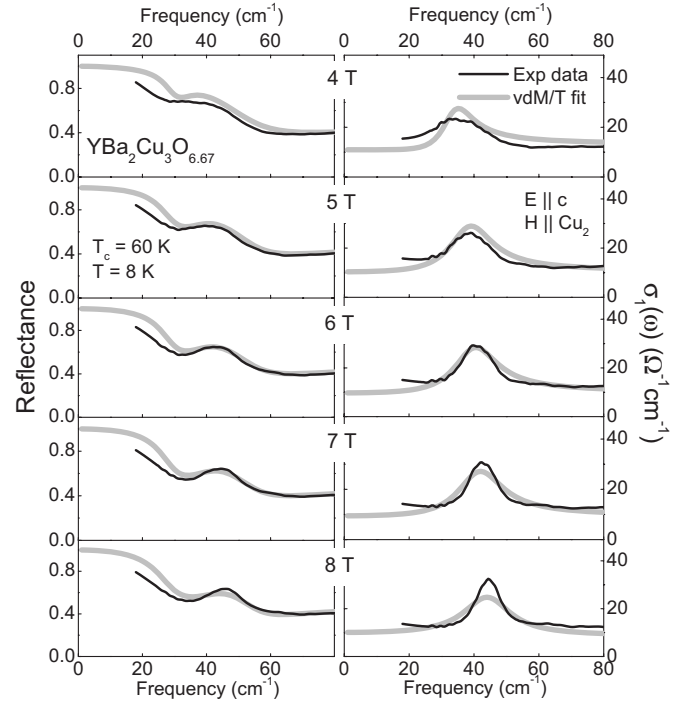


FIG. 11. Fits (thick gray) to experimental reflectance data (thin black) at $T=8 \text{ K}$ and several values of magnetic field using theory of van der Marel and Tvetskov (left panels) and optical conductivity derived from fit function (right panels). These curves from the $y=6.67$ doping are shown as example of the quality of fit which can be obtained. The model was also successful for the sample with $y=6.75$. Fit parameters are displayed in Table II, with the only free parameters being the linewidths γ_a and γ_b . All other parameters were measured directly in the conductivity and loss function or calculated as described in the text.

maintain a constant “center of spectral weight.”

This model yields a good fit to the present YBCO data with few free parameters, and has an excellent track record in describing far-infrared resonances in a variety of systems with multilayer geometries.^{28,68} The strength and versatility of the approach stem from its phenomenological handling of the modification of interlayer Josephson couplings. When augmented with detailed calculations of the Josephson vortex superstructure (discussed below) the vdMT framework provides a qualitative account of differences between magneto-optics data in YBCO and La214 compounds.

C. Josephson vortex lattice ground state calculations

The effect of magnetic field upon a superconducting material depends on the relevant field scales for that particular system. Therefore, to analyze on the same footing the in-field JPR response of different families of cuprates it is imperative to turn to calculations of vortex lattice configuration which account for those scales. Recent studies by Koshelev³⁹ as well as Nonomura and Hu³⁷ have worked within the Lawrence-Doniach model. By minimizing the free energy functional they obtained the Josephson vortex lattice ground state. Here the critical field is defined as $H_{cr} = \Phi_0 / 2\pi\gamma s^2$, where Φ_0 is the magnetic flux quantum, γ is the anisotropy parameter, and s is the interlayer distance. For high fields the Josephson vortices fill every layer to form a dense lattice [Fig. 12(a)], but upon lowering below $H = H_{cr}$ it becomes favorable for each pair of layers containing vortices to be separated by an empty layer [Fig. 12(b)]. As the field is further decreased there is a complicated series of first order transitions between configurations with varying spacings, until a dilute lattice is eventually formed for $H \ll H_{cr}$ [Fig. 12(c)]. For Bi2212, $H_{cr} \approx 0.21$ T ($\gamma = 1100$, $s = 12$ Å), while for YBCO and La214 the field scales are 11 T ($\gamma = 20$, $s = 12$ Å) and 60 T ($\gamma = 13$, $s = 6.4$ Å), respectively.

The limitations on experimentally available magnetic field strength then place each sample in Fig. 8 in a different field regime. In the case of La214, the maximum field experimentally available (17 T) is just over a quarter of H_{cr} , so the vortex structure is still dilute. Thus, the data for La214 would be more accurately compared to the far left side of Fig. 8(e), where the upper frequency mode softens with field and the lower frequency mode is not yet observed. For YBCO, however, H_{cr} is only slightly higher than the upper experimental limit. For this system the low-frequency loss function peak is first resolved just below $H_{cr}/2$, as was observed for Bi2212. The broad onset of this feature in YBCO at fields as low as $H_{cr}/4$ has not yet been reconciled with the single-peaked spectra of La214. Only for Bi2212, which boasts an anisotropy 50–100 times as large as that of YBCO or La214, is the dense vortex lattice regime explored. This information provides justification for the assumptions of vortex superstructure at the core of the vdMT theory. It also allows insight into charging effects, for if the theoretical value of the vortex spacing is inserted into the equation for layer weight factors it is possible to determine the electronic compressibility. Further, these calculations allow for new numerical solutions of the interlayer phase equations³⁸ which will be discussed in Sec. III D.

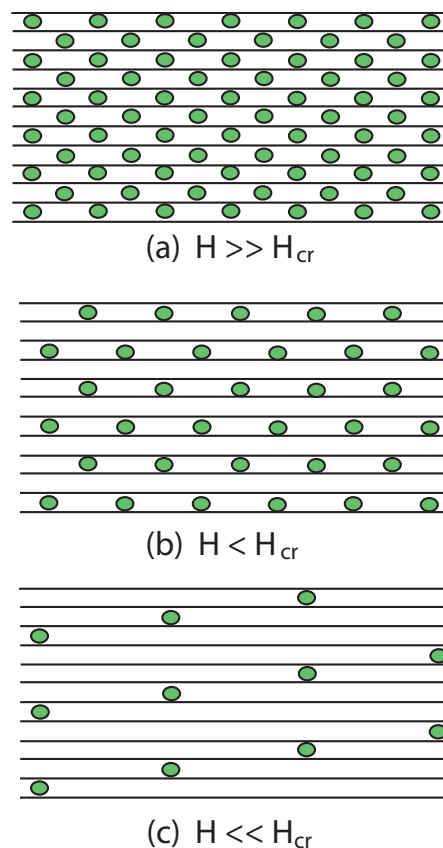


FIG. 12. (Color online) Ground state configuration of Josephson vortex lattice for several values of magnetic field, as predicted by Nonomura and Hu (Ref. 37), and Koshelev (Ref. 39). (a) For fields larger than the critical field scale H_{cr} (see text) vortices form a dense lattice. (b) Below H_{cr} the lattice undergoes a series of first order transitions to configurations in which layers with vortices are separated by N_z planes. (c) For small fields $H \ll H_{cr}$ vortices form a dilute lattice.

D. Numerical solution of interlayer phase equations

Understanding of the Josephson vortex state electrodynamic response has been further advanced by the inclusion of another set of key parameters, the c -axis and in-plane dissipation values. Recently the equations describing phase dynamics in a layered superconductor in parallel field have been solved numerically by Koshelev,³⁸ yielding a solution for the complex dielectric function $\hat{\epsilon}(\omega)$ which is valid for all frequencies and fields. This work begins with the coupled equations for the phase difference and magnetic field in the absence of charging effects.^{57,58} Assuming a vortex lattice configuration with lattice spacing N_z , the static phase equations are solved for a fixed field. This solution is then input into dynamic phase equations to calculate the oscillating phase, and from it the loss function. This description depends strongly upon both the in-plane and c -axis dissipation parameters, $\nu_{ab} = 4\pi\sigma_c / \epsilon_c \omega_p$ and $\nu_c = 4\pi\sigma_{ab} \lambda_{ab}^2 \omega_p / c^2$, which scale roughly as the inverse of the anisotropy. Also critical is the frequency dependence of their relative strengths. Such an approach provides a natural pathway for addressing the differences among cuprate families, and indeed many observed features are reproduced by the theory. For low values of the

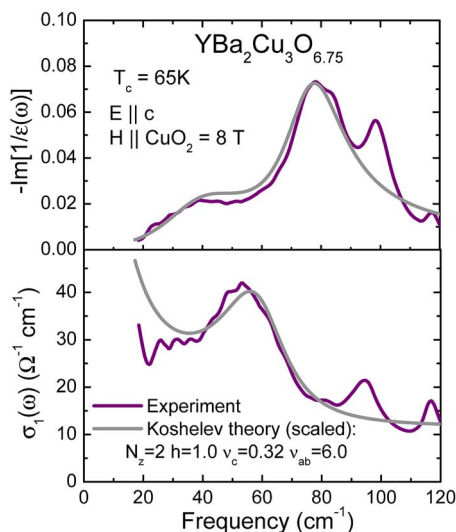


FIG. 13. (Color online) Theoretical loss function and optical conductivity (gray curves) predicted by Koshelev model (Ref. 38) for a system with high dissipation ($\nu_c=0.32, \nu_{ab}=6.0$) in a static magnetic field $h=H/H_{cr}$ (see text). The value of $N_z=2$ refers indicates there are two structural layers between each pair of layers with vortices. Experimental data (purple curves) represent measurements of $\text{YBa}_2\text{Cu}_3\text{O}_{6.75}$ crystals at $T=8$ K and $H=8$ T.

dissipation parameters (typical of those measured in Bi2212), the model matches the field dependence of the two modes measured in that system. And for high dissipation, as realized in underdoped YBCO, fields below H_{cr} generate the observed depletion of the main loss function peak and introduce a low-frequency mode, shown in Fig. 13. The model also exhibits a finite resonance in $\sigma_1(\omega)$ which hardens with magnetic field, in agreement with experimental observations. Here the theoretical curves have been scaled to the plasma frequency and peak heights of the experimental data. Excellent agreement is found in both the linewidths and frequency positions of field-induced modes.

The reliance of this method upon the quasiparticle dissipation initiates a comparison across cuprate families. It is known, for example, that the dc conductivities along the c axis of Bi2212 and YBCO can differ by three orders of

magnitude.⁷¹ Also, the infrared/microwave data for YBCO reveal both a wider JPR linewidth and a stronger frequency dependence of the in-plane optical conductivity than is observed for La214.^{72–74} This model, then, could be exposing the sensitivity of the JPR to these properties.

For completeness, we briefly mention two other structural differences which could contribute to disparities: pinning and layeredness. The CuO chain structure and twin boundaries, which are present only in YBCO, have been shown to affect properties of vortex pinning^{75–77} and may in turn influence the vortex resonance spectra. And of the three systems discussed here, only La214 is single-layered, while YBCO and Bi2212 have two and three layers, respectively. This factor could affect the vortex lattice ground state configuration.

IV. CONCLUSION

In conclusion, we have tracked the electrodynamic response of $\text{YBa}_2\text{Cu}_3\text{O}_{6.67}$ and $\text{YBa}_2\text{Cu}_3\text{O}_{6.75}$ through changes in temperature and magnetic field, paying special attention to the low frequency resonance which appears in the vortex state. In contrast to the in-plane optical properties, which are largely insensitive to magnetic field,⁷⁸ the c -axis response is strongly modified. We have shown that apparent disparities exist in the Josephson vortex state electrodynamic response of several families of cuprate superconductors. After examining proposed theoretical models we can conclude that the differences originate not in variations of vortex mass, but in anisotropy and dissipation. The description proposed by Koshelev³⁸ represents a significant step towards a coherent understanding of the interlayer response of the Josephson vortex state. Future spectroscopic measurements which expand the experimental phase diagram with higher magnetic fields and lower frequencies should further elucidate this subject.⁷⁹

ACKNOWLEDGMENTS

We thank A. E. Koshelev for illuminating discussions and for sharing his drafts prior to publication. This research was supported by the United States Department of Energy and the National Science Foundation. The work done at CRIEPI was supported by the Grant-in-Aid for Science provided by the Japan Society for the Promotion of Science.

*Electronic address: alaforge@physics.ucsd.edu

[†]Present address: Department of Physics, Boston College, 140 Commonwealth Ave., Chestnut Hill, MA 02467, USA.

[‡]Present address: Los Alamos National Laboratory, MS K771, MPA-CINT, Los Alamos, New Mexico 87545, USA.

¹S. L. Cooper and K. E. Gray, in *Physical Properties of High Temperature Superconductors IV*, edited by D. M. Ginsberg (World Scientific, Singapore, 1994) pp. 63–188.

²D. N. Basov and T. Timusk, *Rev. Mod. Phys.* **77**, 721 (2005).

³D. N. Basov, T. Timusk, B. Dabrowski, and J. D. Jorgensen, *Phys. Rev. B* **50**, 3511 (1994).

⁴T. Shibauchi, H. Kitano, K. Uchinokura, A. Maeda, T. Kimura,

and K. Kishio, *Phys. Rev. Lett.* **72**, 2263 (1994).

⁵S. V. Dordevic, E. J. Singley, D. N. Basov, Seiki Komiya, Yoichi Ando, E. Bucher, C. C. Homes, and M. Strongin, *Phys. Rev. B* **65**, 134511 (2002).

⁶M. Reedyk, T. Timusk, J. S. Xue, and J. E. Greedan, *Phys. Rev. B* **49**, 15984 (1994).

⁷J. Schützmann, S. Tajima, S. Miyamoto, Y. Sato, and R. Hauff, *Phys. Rev. B* **52**, 13665 (1995).

⁸C. Bernhard, D. Munzar, A. Golnik, C. T. Lin, A. Wittlin, J. Humlicek, and M. Cardona, *Phys. Rev. B* **61**, 618 (2000).

⁹C. C. Homes, T. Timusk, R. Liang, D. A. Bonn, and W. N. Hardy, *Phys. Rev. Lett.* **71**, 1645 (1993).

- ¹⁰C. C. Homes, T. Timusk, D. A. Bonn, R. Liang, and W. N. Hardy, *Physica C* **254**, 265 (1995).
- ¹¹D. N. Basov, H. A. Mook, B. Dabrowski, and T. Timusk, *Phys. Rev. B* **52**, R13141 (1995).
- ¹²S. Tajima, J. Schützmann, S. Miyamoto, I. Terasaki, Y. Sato, and R. Hauff, *Phys. Rev. B* **55**, 6051 (1997).
- ¹³C. Bernhard, D. Munzar, A. Wittlin, W. König, A. Golnik, C. T. Lin, M. Kläser, Th. Wolf, G. Müller-Vogt, and M. Cardona, *Phys. Rev. B* **59**, R6631 (1999).
- ¹⁴D. Munzar, C. Bernhard, A. Golnik, J. Humlíček, and M. Cardona, *Solid State Commun.* **112**, 365 (1999).
- ¹⁵D. N. Basov, S. I. Woods, A. S. Katz, E. J. Singley, R. C. Dynes, M. Xu, D. G. Hinks, C. C. Homes, and M. Strongin, *Science* **283**, 49 (1999).
- ¹⁶D. N. Basov, C. C. Homes, E. J. Singley, M. Strongin, T. Timusk, G. Blumberg, and D. van der Marel, *Phys. Rev. B* **63**, 134514 (2001).
- ¹⁷A. S. Katz, S. I. Woods, E. J. Singley, T. W. Li, M. Xu, D. G. Hinks, R. C. Dynes, and D. N. Basov, *Phys. Rev. B* **61**, 5930 (1999).
- ¹⁸A. B. Kuzmenko, N. Tombros, H. J. A. Molegraaf, M. Gruninger, D. van der Marel, and S. Uchida, *Phys. Rev. Lett.* **91**, 037004 (2003).
- ¹⁹A. V. Boris, D. Munzar, N. N. Kovaleva, B. Liang, C. T. Lin, A. Dubroka, A. V. Pimenov, T. Holden, B. Keimer, Y.-L. Mathis, and C. Bernhard, *Phys. Rev. Lett.* **89**, 277001 (2002).
- ²⁰Dominik Munzar, Todd Holden, and Christian Bernhard, *Phys. Rev. B* **67**, 020501(R) (2003).
- ²¹K. Tamasaku, Y. Nakamura, and S. Uchida, *Phys. Rev. Lett.* **69**, 1455 (1992).
- ²²T. Timusk and C. C. Homes, *Solid State Commun.* **126**, 63 (2003).
- ²³S. V. Dordevic, E. J. Singley, J. H. Kim, M. B. Maple, Seiki Komiyama, S. Ono, Yoichi Ando, T. Rōm, Ruxing Liang, D. A. Bonn, W. N. Hardy, J. P. Carbotte, C. C. Homes, M. Strongin, and D. N. Basov, *Phys. Rev. B* **69**, 094511 (2004).
- ²⁴A. M. Gerrits, M. E. J. Boonman, A. Wittlin, P. J. M. van Bentum, V. H. M. Duijn, and A. A. Menovsky, *Phys. Rev. B* **51**, 12049 (1995).
- ²⁵S. V. Dordevic, S. Komiyama, Y. Ando, Y. J. Wang, and D. N. Basov, *Phys. Rev. B* **71**, 054503 (2005).
- ²⁶S. V. Dordevic, S. Komiyama, Y. Ando, Y. J. Wang, and D. N. Basov, *Europhys. Lett.* **61**, 122 (2003).
- ²⁷K. M. Kojima, S. Uchida, Y. Fudamoto, and S. Tajima, *Phys. Rev. Lett.* **89**, 247001 (2002).
- ²⁸Diana Dulic, S. J. Hak, D. van der Marel, W. N. Hardy, A. E. Koshelev, Ruixing Liang, D. A. Bonn, and B. A. Willemsen, *Phys. Rev. Lett.* **86**, 4660 (2001).
- ²⁹G. Blatter, M. V. Feigel'man, V. B. Geshkenbein, A. I. Larkin, and V. M. Vinokur, *Rev. Mod. Phys.* **66**, 1125 (1994).
- ³⁰M. Golosovsky, M. Tsindlekht, and D. Davidov, *Semicond. Sci. Technol.* **9**, 1 (1996).
- ³¹S. N. Artemenko, I. G. Gorlova, and Yu. I. Latyshev, *Phys. Lett. A* **138**, 428 (1989).
- ³²W. K. Kwok, J. Fendrich, U. Welp, S. Fleshler, J. Downey, and G. W. Crabtree, *Phys. Rev. Lett.* **72**, 1088 (1994).
- ³³E. Zeldov, D. Majer, M. Konczykowski, V. B. Geshkenbein, M. Vinokur, and H. Shtrikman, *Nature (London)* **375**, 373 (1995).
- ³⁴Y. Matsuda, M. B. Gaifullin, K. Kumagai, K. Kadowaki, and T. Mochiku, *Phys. Rev. Lett.* **75**, 4512 (1995).
- ³⁵M. Tachiki, T. Koyama, and S. Takahashi, *Phys. Rev. B* **50**, 7065 (1994).
- ³⁶D. van der Marel and A. Tsvetkov, *Czech. J. Phys.* **46**, 3165 (1996).
- ³⁷Yoshihiko Nonomura and Xiao Hu, *Phys. Rev. B* **74**, 024504 (2006).
- ³⁸A. E. Koshelev, *Phys. Rev. B* **76**, 054525 (2007).
- ³⁹A. E. Koshelev, arXiv:cond-mat/0602341 (unpublished).
- ⁴⁰L. Bulaevskii and John R. Clem, *Phys. Rev. B* **44**, 10234 (1991).
- ⁴¹L. N. Bulaevskii, V. L. Pokrovsky, and M. P. Maley, *Phys. Rev. Lett.* **76**, 1719 (1996).
- ⁴²M. Ichioka, *Phys. Rev. B* **51**, 9423 (1995).
- ⁴³A. E. Koshelev, L. I. Glazman, and A. I. Larkin, *Phys. Rev. B* **53**, 2786 (1996).
- ⁴⁴Kouji Segawa and Yoichi Ando, *Phys. Rev. B* **69**, 104521 (2004).
- ⁴⁵C. C. Homes, M. Reedyk, D. A. Cradles, and T. Timusk, *Appl. Opt.* **32**, 2976 (1993).
- ⁴⁶W. J. Padilla, Z. Q. Li, K. S. Burch, Y. S. Lee, K. J. Mikolaitis, and D. N. Basov, *Rev. Sci. Instrum.* **75**, 4710 (2004).
- ⁴⁷D. Y. Smith, *Phys. Rev. B* **13**, 5303 (1976).
- ⁴⁸W. J. Padilla, Y. S. Lee, M. Dumm, G. Blumberg, S. Ono, Kouji Segawa, Seiki Komiyama, Yoichi Ando, and D. N. Basov, *Phys. Rev. B* **72**, 060511(R) (2005).
- ⁴⁹Yu. Eltsev and O. Rapp, *Phys. Rev. B* **57**, R3237 (1998).
- ⁵⁰S. V. Dordevic, Seiki Komiyama, Yoichi Ando, and D. N. Basov, *Phys. Rev. Lett.* **91**, 167401 (2003).
- ⁵¹I. Takeya, T. Wada, R. Nakamura, and K. Kadowaki, *Phys. Rev. B* **72**, 014540 (2005).
- ⁵²A. L. Fetter and M. J. Stephen, *Phys. Rev.* **168**, 475 (1968).
- ⁵³T. Koyama, *Phys. Rev. B* **68**, 224505 (2003).
- ⁵⁴A. E. Koshelev and I. Aranson, *Phys. Rev. B* **64**, 174508 (2001).
- ⁵⁵L. N. Bulaevskii, D. Domínguez, M. P. Maley, and A. R. Bishop, *Phys. Rev. B* **55**, 8482 (1997).
- ⁵⁶M. Gruninger, D. van der Marel, A. A. Tsvetkov, and A. Erb, *Phys. Rev. Lett.* **84**, 1575 (2000).
- ⁵⁷S. N. Artemenko and S. V. Remizov, *JETP Lett.* **66**, 853 (1997).
- ⁵⁸A. E. Koshelev and I. Aranson, *Phys. Rev. B* **64**, 174508 (2001).
- ⁵⁹A. E. Koshelev, L. N. Bulaevskii, and M. P. Maley, *Phys. Rev. B* **62**, 14403 (2000).
- ⁶⁰Yoichi Ando and Kouji Segawa, *Phys. Rev. Lett.* **88**, 167005 (2002).
- ⁶¹J. R. Clem and M. W. Coffey, *Phys. Rev. B* **42**, 6209 (1990).
- ⁶²Mark W. Coffey and John R. Clem, *Phys. Rev. B* **44**, 6903 (1991).
- ⁶³D. M. Gaitonde and T. V. Ramakrishnan, *Phys. Rev. B* **56**, 11951 (1997).
- ⁶⁴Lorenz Bartosch, Leon Balents, and Subir Sachdev, arXiv:cond-mat/0502002 (unpublished).
- ⁶⁵Kathryn A. Moler, Alexander L. Fetter, and Aharon Kapitulnik, *J. Low Temp. Phys.* **100**, 185 (1995).
- ⁶⁶H. Shibata and T. Yamada, *Phys. Rev. Lett.* **81**, 3519 (1998).
- ⁶⁷Diana Dulic, A. Pimenov, D. van der Marel, D. M. Broun, Saied Kamal, W. N. Hardy, A. A. Tsvetkov, I. M. Sutjaha, Ruixing Liang, A. A. Menovsky, A. Loidl, and S. S. Saxena, *Phys. Rev. Lett.* **86**, 4144 (2001).
- ⁶⁸A. Pimenov, A. Loidl, D. Dulic, D. van der Marel, I. M. Sutjaha, and A. A. Menovsky, *Phys. Rev. Lett.* **87**, 177003 (2001).
- ⁶⁹D. van der Marel and A. A. Tsvetkov, *Phys. Rev. B* **64**, 024530 (2001).

- ⁷⁰Ch. Helm, L. N. Bulaevskii, E. M. Chudnovsky, and M. P. Maley, *Phys. Rev. Lett.* **89**, 057003 (2002).
- ⁷¹P. J. Thomas, J. C. Fenton, G. Yang, and C. E. Gough, arXiv:cond-mat/0001365 (unpublished).
- ⁷²M. Dumm, D. N. Basov, Seiki Komiya, Yasushi Abe, and Yoichi Ando, *Phys. Rev. Lett.* **88**, 147003 (2002).
- ⁷³J. Hwang, J. Yang, T. Timusk, S. G. Sharapov, J. P. Carbotte, D. A. Bonn, Ruixing Liang, and W. N. Hardy, *Phys. Rev. B* **73**, 014508 (2006).
- ⁷⁴A. Hosseini, R. Harris, S. Kamal, P. Dosanjh, J. Preston, R. Liang, W. N. Hardy, and D. A. Bonn, *Phys. Rev. B* **60**, 1349 (1999).
- ⁷⁵Y.-S. Lee, Kouji Segawa, Yoichi Ando, and D. N. Basov, *Phys. Rev. B* **70**, 014518 (2004).
- ⁷⁶E. M. Gyorgy, R. B. van Dover, L. F. Schneemeyer, A. E. White, H. M. O'Bryan, R. J. Felder, J. V. Waszczak, W. W. Rhodes, and F. Hellman, *Appl. Phys. Lett.* **56**, 2465 (1990).
- ⁷⁷J. A. Herbsommer, G. Nieva, and J. Luzuriaga, *Phys. Rev. B* **62**, 3534 (2000).
- ⁷⁸Y. S. Lee, Z. Q. Li, W. J. Padilla, S. V. Dordevic, C. C. Homes, Kouji Segawa, Yoichi Ando, and D. N. Basov, *Phys. Rev. B* **72**, 172511 (2005).
- ⁷⁹P. J. Turner, R. Harris, Saeid Kamal, M. E. Hayden, D. M. Broun, D. C. Morgan, A. Hosseini, P. Dosanjh, G. K. Mullins, J. S. Preston, Ruixing Liang, D. A. Bonn, and W. N. Hardy, *Phys. Rev. Lett.* **90**, 237005 (2003).